Check for updates

Advanced Materials

ADVANCED MATERIALS
www.advmat.de

RESEARCH ARTICLE

Multi-Anion Electrocatalysts Stabilized by Anionic Configurational Entropy for Advanced Water Splitting

Wei Liao | Hai-Liang Su | Shao-Xin Mo | Yonghai Cao | Hongjuan Wang | Hao Yu | Hao-Fan Wang

School of Chemistry and Chemical Engineering, South China University of Technology, Guangzhou, P. R. China

Correspondence: Hao-Fan Wang (whf@scut.edu.cn)

Received: 4 January 2026 | **Revised:** 9 February 2026 | **Accepted:** 4 March 2026

Keywords: anionic configurational entropy | electrocatalysis | medium- and high-entropy materials | multi-anion compounds | water splitting

ABSTRACT

Anion regulation in transition metal compounds provides an effective strategy to modulate their electrocatalytic activity. However, the coexistence of multiple anions often results in thermodynamically favored phase separation, restricting the density and tunability of active sites. To address this limitation, we draw inspiration from the high-entropy strategy, where configurational entropy promotes uniform elemental mixing and is predominantly applied in multi-metal systems. Here, we extend this design to anion regulation, employing diverse anionic components to enhance configurational entropy, suppress the enthalpy-driven phase separation, and achieve thermodynamically stable single-phase structures. The atomic-level anion homogeneity thereby enables precise modulation of the electronic structure of metal sites. As a proof of concept, a multi-anion electrocatalyst containing hydroxide, sulfide, selenide, and phosphate anions is successfully synthesized and achieves low overpotentials of 25 mV for hydrogen evolution and 146 mV for oxygen evolution at 10 mA cm^{-2}. When integrated into an anion-exchange membrane water electrolyzer, the catalyst delivers a current density of 1,000 mA cm^{-2} at 1.98 V and maintains stable operation for 200 h at 25 °C. Focusing on anionic configurational entropy, this study thermodynamically stabilizes conventionally metastable multi-anion compounds, broadens the scope of medium/high-entropy materials, and provides guidance for the design of next-generation electrocatalysts.

1 | Introduction

In the context of the accelerating global shift toward carbon neutrality, green hydrogen has emerged as a pivotal zero-carbon energy carrier, offering promising solutions to both the energy crisis and environmental challenges [1–3]. Water electrolysis technology enables the conversion of renewable energy into high-purity hydrogen through the cathodic hydrogen evolution reaction (HER) and anodic oxygen evolution reaction (OER) [4–7]. However, its industrial deployment remains constrained by significant energy losses arising from high overpotentials [8–10]. Commercial electrolyzers still rely on precious metal catalysts (e.g., Pt/C and RuO_2), whose material expenses represent a substantial portion of the system cost and suffer from limited long-term durability [11–13]. Therefore, the development of highly active and stable non-precious metal catalysts for both HER and OER has become increasingly critical, as they offer a promising pathway to reduce material costs and improve the scalability of water electrolysis technology [14–17, 8, 18].

In the field of transition metal-based electrocatalysts, nickel-based compounds have attracted sustained attention due to their tunable 3d electronic configurations and cost-effective nature [19–22]. Among the various structural factors, anions such as S, Se and P play a crucial role in tuning the electronic configuration of Ni centers, thereby affecting the adsorption behavior of key intermediates and ultimately influencing catalytic performance [23–28]. For instance, Both Liu et al. [29] and Popczun

© 2026 Wiley-VCH GmbH

et al. [30] demonstrated that the incorporation of P modulates the electronic structure of Ni, optimizes the adsorption strength of hydrogen intermediates, and significantly enhances the HER activity of Ni_2P catalysts. However, the regulation of hydrogen adsorption energy at metal sites by a single anion can be either overly strengthened or excessively weakened, resulting in low HER activity. Meng et al. [31] reported that the H adsorption free energies of NiS and NiSe are −0.33 and 0.45 eV respectively, both far from the optimal value (0 eV) for HER. In contrast, incorporating both Se and S anions tunes the value to 0.22 eV and improves HER activity. Thus, co-doping two or more anions into metal compounds enables more precise tuning of the metal electronic structure through differences in anionic properties, thereby optimizing the adsorption energies of reaction intermediates [32–37]. However, the large differences in the physicochemical properties of various anions often result in phase separation and the formation of thermodynamically stable multiphase structures [38, 39]. Such phase separation typically causes non-uniform anion distribution, where only the metal sites at the phase interface benefit from multi-anion regulation, while regions farther from the interface retain single-anion characteristics, resulting in uneven catalytic activity and limited overall performance [40, 41]. In addition, the fixed composition of anions in such multiphase structures further limits the overall structural tunability. These issues reflect the fundamental limitation of conventional mixed-anion strategies, namely that localized electronic optimization fails to improve the overall performance of active sites, thereby highlighting the urgent need for new strategies to overcome this bottleneck.

In recent years, the concept of high-entropy materials (such as high-entropy alloys/oxides/hydroxides) has emerged, which offers an effective strategy to promote multicomponent metal mixing by increasing the number of metal elements and enhancing cationic configurational entropy [42–47]. The configurational entropy for systems involving cationic and anionic sublattices can be expressed as:

$$\Delta S_{\text{config}} = -R\left[\left(\sum_{a=1}^{m} x_a \ln x_a\right)_{\text{cation}} + \left(\sum_{b=1}^{n} x_b \ln x_b\right)_{\text{anion}}\right] \quad (1)$$

where x_a and x_b represent the atomic fractions of the components on the cationic and anionic sublattices, respectively; m and n are the numbers of cation and anion types; and R is the gas constant. In typical high-entropy materials such as high-entropy alloys or high-entropy oxides, which contain no anions or only one type of anion, the configurational entropy arises entirely from the diversity of metal elements. As shown in Equation 1, increasing the number of metal components leads to a higher configurational entropy in the uniformly mixed state, resulting in a larger entropy change (ΔS_{mix}) during mixing. The stability of a mixed phase can be evaluated using the Gibbs free energy criterion of mixing:

$$\Delta G_{\text{mix}} = \Delta H_{\text{mix}} - T\Delta S_{\text{mix}} \quad (2)$$

At sufficiently high entropy levels, the negative entropy term can offset unfavorable enthalpy contributions, thereby lowering the overall free energy and stabilizing a single-phase structure with uniform elemental distribution.

While previous high-entropy materials have focused exclusively on metal mixing, it is revealed in Equation 1 that anions contribute equally to the overall configurational entropy. Building on this insight, we propose an anionic entropy engineering strategy by enhancing configurational entropy through multi-anion incorporation. This approach overcomes the enthalpy-driven tendency for phase separation and enables the formation of a stable single-phase compound with uniform anion distribution, offering a promising yet underexplored direction for the innovative design of medium- and high-entropy materials. We define such materials, where diverse anions randomly occupy the same type of lattice sites without phase separation, as multi-anion compounds [48].

In this work, the feasibility of constructing multi-anion compounds by increasing anionic configurational entropy is first validated using a simple single-metal compound model as a proof of concept. Based on the structure of $Ni(OH)_2$, the doping of sulfur, selenium, and phosphorus ions increases the configurational entropy (up to 1.33R in the NiSSeP(OH) model). Theoretical calculations show that the increased entropy offsets the enthalpic driving force for phase separation, enabling the formation of a thermodynamically favored single-phase structure. Experimental characterizations also confirm the uniform mixing of anions, which enables consistent regulation of the Ni electronic environment throughout the system, leading to enhanced HER and OER activity. To further improve catalytic activity while demonstrating the applicability of this entropy-driven strategy to more complex systems, a trimetallic precursor was constructed to synthesize a single-phase NiFeZn-SSeP(OH) compound anchored on nickel foam (NiFeZn-SSeP(OH)/NF). The configurational entropy of this system reaches 2.15R, with anionic contribution accounting for 1.31R, ensuring the formation of a homogeneous solid solution. The uniform distribution of multiple metals and anions collectively tunes the Ni electronic structure, resulting in a remarkable improvement in both HER and OER performance. As a result, NiFeZn-SSeP(OH)/NF achieves overpotentials of just 25 mV for HER and 146 mV for OER at 10 mA cm^{-2}, and delivers a current density of 1,000 mA cm^{-2} at 1.98 V in an anion exchange membrane (AEM) water electrolyzer at 25 °C, with stable operation maintained for over 200 h. This work extends the concept of high-entropy materials to multi-anion compounds by utilizing the anionic configurational entropy to overcome enthalpy-driven phase separation and achieve uniform anion incorporation. Such an approach leads to the formation of single-phase multi-anion compounds with enhanced electrocatalytic water splitting performance, and offers a broadly applicable design principle for high-performance materials across diverse application fields.

2 | Results and Discussion

2.1 | Validation of Entropy-Driven Multi-Anion Mixing in Model System

To validate the feasibility of constructing multi-anion compounds through enhanced anionic configurational entropy, we constructed a theoretical crystal model of nickel hydroxide ($Ni(OH)_2$) and substituted hydroxyl groups with S, Se, and P anions, yielding a series of representative multi-anion structural models with

15214095, 2026, 20, Downloaded from https://advanced.onlinelibrary.wiley.com/doi/10.1002/adma.72791 by Yonghai Cao - South China University Of Technology , Wiley Online Library on [17/11/2026]. See the Terms and Conditions (https://onlinelibrary.wiley.com/terms-and-conditions) on Wiley Online Library for rules of use; OA articles are governed by the applicable Creative Commons License

equimolar anion compositions. The S, Se, and P anions were selected based on their well-established roles in electrocatalysis and broad ranges of electronegativity and ionic size, which are expected to enable precise tuning of the Ni-site electronic structure. These configurations include dual-anion (e.g., NiS(OH)), ternary-anion (e.g., NiSSe(OH)), and quaternary-anion (NiSSeP(OH)) systems. For models with uniformly distributed anions, the configurational entropy was calculated based on Equation 1, while that of phase-separated models was set to zero. For instance, the NiSSeP(OH) model with uniformly distributed S, Se, P, and hydroxide anions exhibits a configurational entropy of 1.33*R*. To evaluate the thermodynamic stability of these structures, Gibbs free energies of formation (ΔG_f) were calculated using density functional theory (DFT) based on Equation 2 and Figures S1–S3, incorporating both the vibrational entropy at 130 °C and the corresponding configurational entropy [49]. As shown in Figure 1a, the single-phase NiSSeP(OH) model with uniformly distributed anions ($\Delta G_f = -4.01$ eV) is thermodynamically favored over the phase-separated state ($\Delta G_f = -2.81$ eV). This preference primarily arises from the configurational entropy contribution (−2.87 eV), indicating that configurational entropy gain from homogeneous multi-anion incorporation effectively offsets the enthalpy cost of anion mixing. In contrast, for fewer-anion systems such as NiS(OH) and NiSSe(OH), the ΔG_f values of the multi-phase models are lower than those of the corresponding single-phase models, suggesting a thermodynamic tendency toward phase separation when configurational entropy is insufficient. Therefore, enhancing anionic configurational entropy provides a thermodynamically viable route to suppress phase separation in mixed-anion systems and enables the formation of homogeneous multi-anion structures. This anion entropy increase-induced stabilization is schematically illustrated in Figure 1b and Figure S1, where the increase in entropy offsets the unfavorable enthalpy and drives the system from a phase-separated to a single-phase state [50]. To evaluate the reasonableness of the multi-anion compound model, we further constructed a series of NiSSeP(OH) supercells with different anion distributions. As shown in Figure S2, in addition to the previously mentioned random configuration (NiSSeP(OH)), another randomized model, denoted NiSSeP(OH)-1, was also generated. To explore the effects of increasing local anion ordering, we further constructed four locally ordered models in which each coordination sphere of Ni contains 2, 3, 4, or 5 identical anions to the maximum extent allowed by the cell (NiSSeP(OH)-2/-3/-4/-5). The fully phase-separated model described above is hereafter referred to as NiSSeP(OH)-6. The total-energy trend follows NiSSeP(OH) ≈ NiSSeP(OH)-1< NiSSeP(OH)-2< NiSSeP(OH)-3< NiSSeP(OH)-4< NiSSeP(OH)-5< NiSSeP(OH)-6, indicating that the clustering of identical anions is energetically disfavored, whereas the different randomly mixed anion arrangements exhibit essentially the same low energy. Moreover, density-of-states analysis shows that the two random multi-anion models possess nearly identical d-band centers, suggesting comparable electronic structures. Taken together, the energetic and electronic-feature analyses demonstrate that different random configurations are essentially equivalent in stability and activity. This validates the use of a single random configuration as representative of the mixed-anion system.

To further investigate the functional role of anions in tuning catalytic activity, hydrogen adsorption (H*) energies were calculated at Ni active sites for different anion surroundings (Figure S3). As shown in Figure 1c, the pristine $Ni(OH)_2$ shows weak H* adsorption (1.60 eV), while single-anion substitutions provide limited modulation. In contrast, the multi-anionic NiSSeP(OH) configuration exhibits a nearly thermoneutral adsorption energy (0.393 eV), indicative of its enhanced HER performance [51].

Encouraged by these theoretical results, we synthesized a multi-anion compound NiSSeP(OH)/NF using $Ni(OH)_2$/NF as the precursor via a one-step hydrothermal ion-exchange process, in which S, Se, and P anions were introduced with carefully controlled feeding ratios. Given the varying affinities of Ni toward different anions (Se > P > S, see Figure S4), the anion feed ratios were tuned to balance the Ni-anion interactions, thereby yielding products with near-uniform anion distribution. In practice, P is introduced as red phosphorus and converted in situ into PH_3 as the reactive P source for anion exchange. Due to the limited conversion efficiency, an excess amount of P was supplied, giving a feed molar ratio of S:Se:P = 2:0.5:3. The composition of the product was determined using inductively coupled plasma optical emission spectroscopy (ICP-OES) and area-averaged energy dispersive spectroscopy (EDS) (Table S1). The ICP-OES-measured content (S: 5.30 wt.%, Se: 13.31 wt.%, P: 2.29 wt.%) was consistent with the EDS results (S: 6.92 wt.%, Se: 13.88 wt.%, P: 3.76 wt.%). The morphology of the multi-anion compound was first examined using scanning electron microscopy (SEM) and transmission electron microscopy (TEM). As shown in Figure 1d–g, the $Ni(OH)_2$/NF precursor exhibits a flower-like microspherical structure composed of vertically stacked nanosheets. After the incorporation of multiple anions, NiSSeP(OH)/NF retains a similar architecture, indicating that the overall morphology is preserved during the anion exchange process. EDS mapping (Figures S5 and S6) confirms the uniform spatial distribution of S, Se, and P across the nanosheets, excluding the occurrence of element aggregation or phase separation at the microscale. Moreover, electrochemical measurements revealed a progressive improvement in HER and OER activity with increasing anionic configuration entropy (Figure 1h,i). NiSSeP(OH)/NF exhibited the lowest overpotentials of 105 mV (HER) and 225 mV (OER) at 10 mA cm^{-2}, significantly outperforming materials with lower anionic entropy, thereby confirming the catalytic benefits of uniform multi-anion coordination. In summary, based on a single-metal model system, we successfully demonstrate the feasibility of constructing single-phase multi-anion compounds through increasing anionic configurational entropy, and confirm that the multi-anion configuration effectively enhances the catalytic activity.

2.2 | Synthesis and Characterization of High-Activity Multi-Anion Electrocatalyst

Building upon the concept validated in the monometallic Ni-based system, the anion configurational entropy strategy was further extended to a NiFeZn trimetallic platform, with the aim of further enhancing electrocatalytic activity through broader electronic modulation. The target compound, NiFeZn-SSeP(OH)/NF, was synthesized via a method analogous to that used for NiSSeP(OH)/NF. As illustrated in Figure 2a, a NiFeZn layered double hydroxide (NiFeZn-LDH) precursor was first grown on nickel foam, followed by immersion in a pre-mixed solution containing

15214095, 2026, 20, Downloaded from https://advanced.onlinelibrary.wiley.com/doi/10.1002/adma.72791 by Yonghai Cao - South China University Of Technology , Wiley Online Library on [17/11/2026]. See the Terms and Conditions (https://onlinelibrary.wiley.com/terms-and-conditions) on Wiley Online Library for rules of use; OA articles are governed by the applicable Creative Commons License

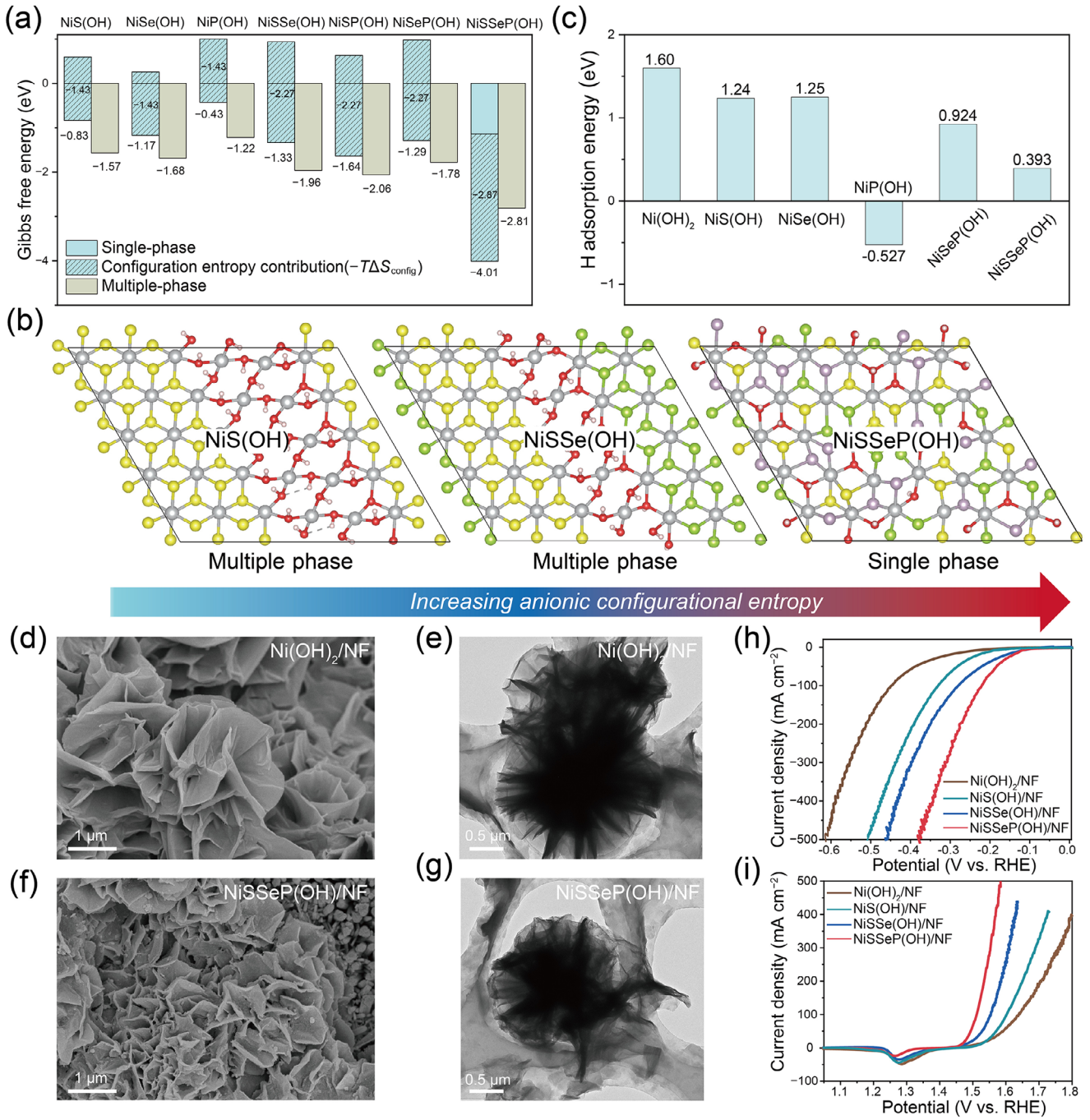

FIGURE 1 | (a) Gibbs free energies of formation of single-phase and multiphase structures for various anion-doped models. (b) Schematic illustration of the entropy-driven stabilization effect on Ni-based multi-anion systems. (c) Calculated hydrogen adsorption energies on different multi-anion models. (d) SEM and (e) TEM images of $Ni(OH)_2$/NF. (f) SEM and (g) TEM images of NiSSeP(OH)/NF. Polarization curves for (h) HER and (i) OER of $Ni(OH)_2$/NF, NiS(OH)/NF, NiSSe(OH)/NF, and NiSSeP(OH)/NF measured in 1.0 M KOH.

S, Se, and P anions and subsequent hydrothermal treatment at 130°C for 12 h (see Supporting Information for details). To examine the morphological and structural features of the resulting multi-anion compound, SEM and TEM analyses were carried out. As shown in Figure 2b,f, the NiFeZn-LDH precursor exhibits a typical nanosheet morphology that remains well preserved after multi-anion incorporation, indicating high structural robustness during the entire process. TEM images (Figure 2c,g) further confirm the retention of the ultrathin nanosheet architecture. Additionally, high-resolution TEM (HRTEM, Figure 2d,h) images reveal lattice spacings of 0.266 nm and 0.268 nm for the precursor and the final product, respectively, both corresponding to the (101) planes of NiFe-LDH (PDF#40-0215), demonstrating that the layered crystal structure is maintained after multi-anion substitution. Consistent with these results, the selected-area electron diffraction (SAED) patterns (Figure 2e,i) exhibit similar diffraction rings before and after the anion exchange process, further confirming the preservation of the single-phase crystalline structure. To investigate the spatial distribution of the anions, EDS mapping was performed on NiFeZn-SSeP(OH)/NF.

15214095, 2026, 20, Downloaded from https://advanced.onlinelibrary.wiley.com/doi/10.1002/adma.72791 by Yonghai Cao - South China University Of Technology , Wiley Online Library on [17/11/2026]. See the Terms and Conditions (https://onlinelibrary.wiley.com/terms-and-conditions) on Wiley Online Library for rules of use; OA articles are governed by the applicable Creative Commons License

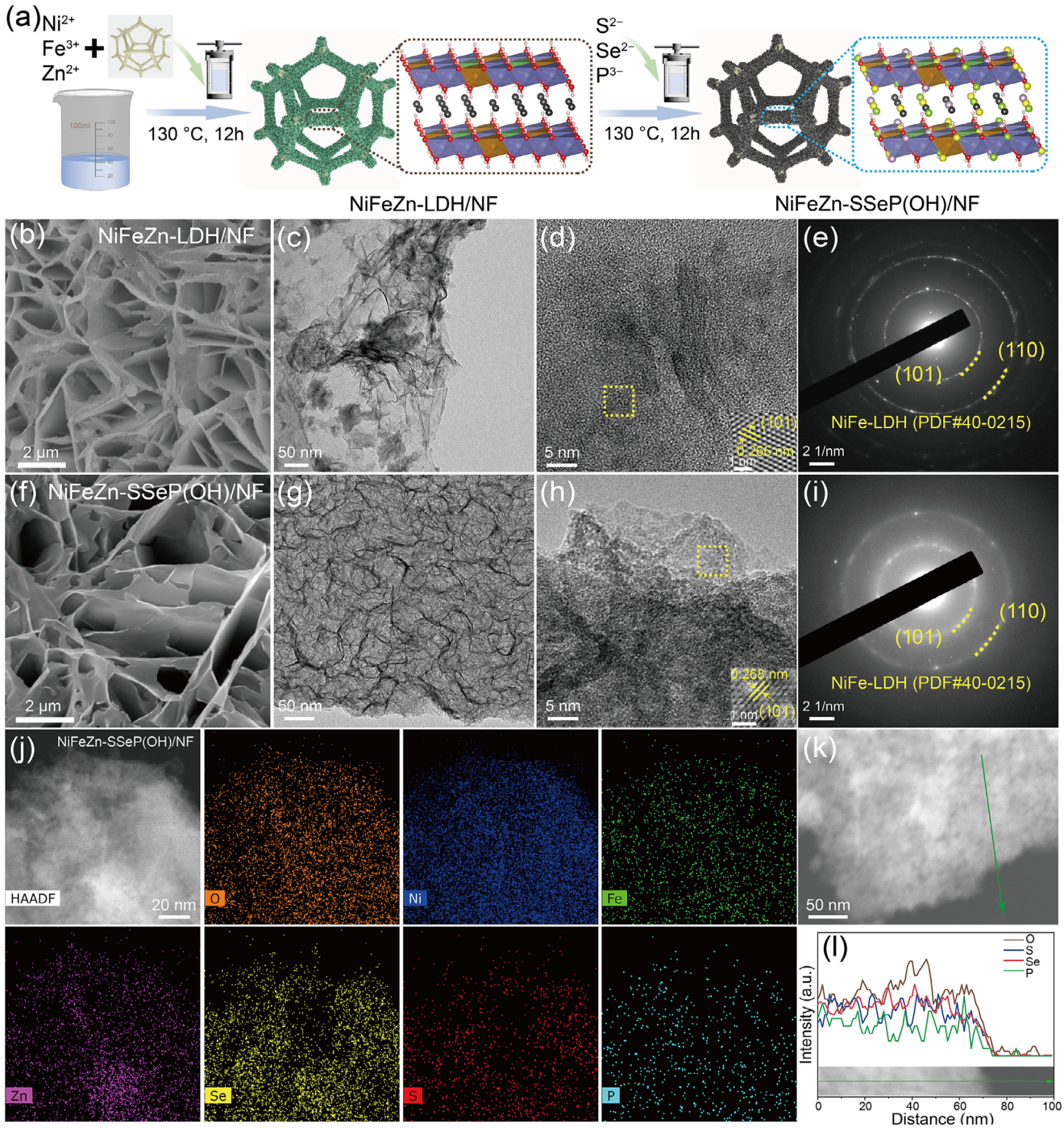

FIGURE 2 | (a) Schematic illustration of the synthesis of NiFeZn-SSeP(OH)/NF. SEM, TEM, HRTEM, and SAED images of (b–e) NiFeZn-LDH/NF and (f–i) NiFeZn-SSeP(OH)/NF. (j) HAADF image and corresponding elemental mapping images of NiFeZn-SSeP(OH)/NF. (k) EDS line-scan image and (l) corresponding elemental intensity profiles.

As shown in Figure 2j, S, Se, and P anions are homogeneously distributed across the nanosheets. HAADF-STEM line-scan analysis (Figure 2k) and the corresponding intensity profile (Figure 2l) further verify elemental uniformity at the nanoscale, with no evidence of local aggregation of any anionic species. Furthermore, SEM-based elemental mapping (Figures S7 and S8) also confirmed that metals and anions were uniformly distributed throughout the material. We quantified the anion composition by ICP-OES together with area-averaged EDS. As shown in Table S2 and S3, ICP-OES analysis revealed that the S content was 4.28 wt.%, the Se content was 12.89 wt.%, and the P content was 1.87 wt.%. These values are in high agreement with the regional average EDS results (S: 4.86 wt.%; Se: 12.47 wt.%; P: 2.22 wt.%), jointly confirming that multiple anions were successfully and uniformly incorporated into the framework.

To evaluate the role of anionic configurational entropy in maintaining structural stability, materials with one or two additional anions incorporated in the precursor were synthesized for comparison. As shown in Figure S9, incorporating either a single

15214095, 2026, 20, Downloaded from https://advanced.onlinelibrary.wiley.com/doi/10.1002/adma.72791 by Yonghai Cao - South China University Of Technology , Wiley Online Library on [17/11/2026]. See the Terms and Conditions (https://onlinelibrary.wiley.com/terms-and-conditions) on Wiley Online Library for rules of use; OA articles are governed by the applicable Creative Commons License

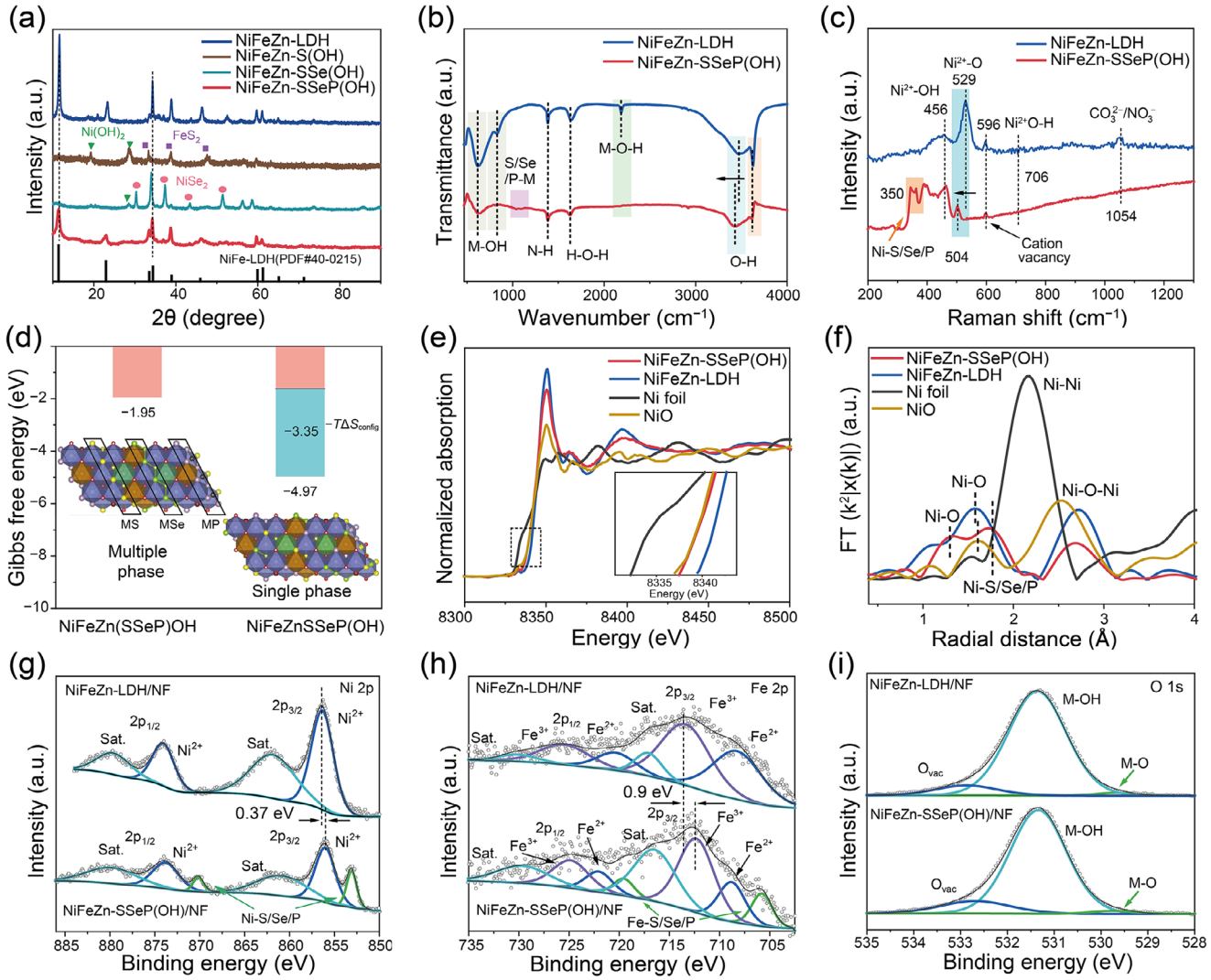

FIGURE 3 | (a) XRD patterns, (b) FTIR spectra, and (c) Raman spectra of NiFeZn-LDH and NiFeZn-SSeP(OH). (d) Calculated Gibbs free energies of single-phase and multiphase structures for the NiFeZnSSeP(OH) model. (e) Ni K-edge XANES spectra and (f) Fourier-transformed Ni K-edge EXAFS spectra of NiFeZn-SSeP(OH). High-resolution XPS spectra of NiFeZn-LDH/NF and NiFeZn-SSeP(OH)/NF: (g) Ni 2p, (h) Fe 2p, and (i) O 1s.

type (S, Se, or P) or binary pairs of these anions induced severe morphological degradation. This disruption stems from limited entropy gain failing to overcome unfavorable enthalpic interactions generated by anion mixing, triggering phase separation and heterogeneous phase formation. In stark contrast, simultaneous incorporation of S, Se, and P preserves the homogeneous nanosheet morphology. This demonstrates that enhanced anion configurational entropy from the coexistence of four types of anions is essential for stabilizing the pristine precursor structure. In summary, preliminary structural characterizations confirm that the entropy-driven multi-anion incorporation strategy is not only effective in monometallic systems but also readily applicable to trimetallic platforms, enabling homogeneous anion distribution and structural preservation, and thereby laying a solid foundation for improved catalytic performance.

The multi-anion compound was further characterized by X-ray diffraction (XRD), Fourier transform infrared (FTIR) spectroscopy, and Raman spectroscopy to demonstrate the uniform distribution of multiple anions within a single-phase lattice. Powder XRD patterns (Figure 3a) reveal that the diffraction peaks of both NiFeZn-LDH and NiFeZn-SSeP(OH) match the standard NiFe-LDH phase (PDF#40-0215), indicating that the incorporation of multiple anions does not alter the LDH crystal structure. In contrast, NiFeZn-S(OH) and NiFeZn-SSe(OH) display additional diffraction peaks of secondary phases, suggesting that lower anionic entropy tends to induce phase separation. Importantly, the enlarged view of XRD patterns (Figure S10a) shows that the diffraction peaks of NiFeZn-SSeP(OH) belonging to the (101) plane are slightly negatively shifted relative to NiFeZn-LDH, indicating that the incorporation of multiple anions causes moderate lattice expansion. Furthermore, Rietveld refinement was performed, yielding lattice parameters of $a = b = 3.0996$ Å and $c = 23.2681$ Å for NiFeZn-SSeP(OH), which are expanded compared with those of NiFeZn-LDH with $a = b = 3.0891$ Å and $c = 22.8711$ Å, confirming lattice expansion while preserving the LDH-type framework (Figure S10b,c). Moreover, XRD patterns of as-synthesized NF-supported samples (Figure S11) also display NiS and NiSe peaks in fewer-anion systems, while the multi-anion NiFeZn-SSeP(OH)/NF remains a

15214095, 2026, 20, Downloaded from https://advanced.onlinelibrary.wiley.com/doi/10.1002/adma.72791 by Yonghai Cao - South China University Of Technology , Wiley Online Library on [17/11/2026]. See the Terms and Conditions (https://onlinelibrary.wiley.com/terms-and-conditions) on Wiley Online Library for rules of use; OA articles are governed by the applicable Creative Commons License

single-phase structure. In addition, multi-anion samples synthesized at different hydrothermal temperatures (Figure S12) show no emergence of new diffraction peaks, further indicating that the high anionic configurational entropy effectively suppresses phase separation and stabilizes uniform anion distribution within the lattice. To further verify the thermodynamic stability of the multi-anion compound, the hydrothermal synthesis process was extended to 24 h. As shown in Figure S13, XRD and SEM results confirm that the LDH crystal structure, nanosheet morphology, and elemental homogeneity remain unchanged. This consistency demonstrates that the entropy-stabilized multi-anion compound is thermodynamically robust rather than a metastable phase.

Further insights into the anionic bonding environment were obtained through FTIR spectroscopy (Figure 3b), which reveals characteristic absorption bands of hydroxides at 1630 cm^{-1} (H—O—H bending vibration) and 3400 cm^{-1} (M—OH stretching) for both NiFeZn-LDH and NiFeZn-SSeP(OH). Additionally, a new band at 1050 cm^{-1} corresponding to S/Se/P–metal bonding is observed after anion incorporation [52]. In the Raman spectrum (Figure 3c) of NiFeZn-SSeP(OH), the intense peak observed around 350 cm^{-1} is attributed to coupled metal–O/(S/Se/P) vibrational modes, whose pronounced enhancement relative to the oxygen-only NiFeZn LDH confirms the dominant contribution of metal–(S/Se/P) bonding [53–55]. While the broad band associated with LDH lattice vibrations between 456 and 530 cm^{-1} remains unchanged [56, 57]. In addition, a defect-related band in the ~596 cm^{-1} region is evident, consistent with cation-vacancy by trace Zn in multi-anion LDHs, which may modulate the local electronic structure and accessible active sites [58]. These results collectively confirm the successful construction of a single-phase multi-anion compound with a preserved LDH framework.

To theoretically verify that high anionic configurational entropy thermodynamically stabilizes uniform anion mixing in this system, we extended the formation Gibbs free energy calculations previously performed for a single-metal model to multi-metal configurations. It is worth noting that since the proportion of cations is fixed, while anions only occupy anion sites in the crystal lattice, we only consider the anion configuration entropy in the calculation of formation free energy. Following the same approach used for the NiSSeP(OH) system, the theoretical anionic configurational entropy of the single-phase model was calculated to be 1.34*R*, while that of the multiphase configuration was assumed to be zero. As shown in Figure 3d, the calculated formation Gibbs free energy of the single-phase NiFeZn-SSeP(OH) is −4.97 eV (including a configurational entropy contribution of −3.35 eV), which is significantly lower than that of the multiphase structure (−1.95 eV). This suggests that high anionic entropy thermodynamically favors the formation of a single-phase structure with uniformly distributed anions.

With the crystal structure confirmed, attention was then directed to elucidating the electronic structure and local coordination environment of the multi-anion compound. As shown in the Ni K-edge X-ray absorption near edge structure (XANES) spectra (Figure 3e), a distinct negative shift is observed for NiFeZn-SSeP(OH) relative to the NiFeZn-LDH precursor, indicating a decrease in the Ni valence state [59]. This can be attributed to the replacement of hydroxyl groups by lower-electronegativity S, Se, and P anions, which modify the local electronic surroundings of the Ni sites. The extended X-ray absorption fine structure (EXAFS) spectrum (Figure 3f) of NiFeZn-SSeP(OH) reveals a pronounced coordination peak at approximately 1.6 Å, consistent with Ni–S/Se/P bonding, thereby confirming the formation of a heterogeneous multi-anion coordination environment [25, 60, 61]. We further performed refined fitting of the Ni K-edge EXAFS spectra to quantify changes in the Ni coordination environment in the multi-anion compounds. The *R*-space and *k*-space fitting results are shown in Figure S14, and the detailed fitting parameters are summarized in Table S4. For the NiFeZn-LDH precursor, the coordination number for the Ni—O path is approximately 5.75, and that for the Ni—O—M path (M = Ni/Fe/Zn) is approximately 5.87, which is consistent with a sixfold octahedral environment around Ni. After multi-anion exchange, the first coordination shell around Ni in NiFeZn-SSeP(OH) changes markedly and contains both Ni—O with a coordination number of ~2.12 and Ni—S/Se/P with a coordination number of ~3.98, giving a total close to six. In the second shell, a Ni—S/Se/P—M path with a coordination number of ~3.76 is also resolved. These fitting results provide direct structural evidence that multiple anions are successfully incorporated into the lattice and form a uniform mixed-coordination environment, strongly supporting our conclusion that anion configurational entropy stabilizes a single-phase framework.

Complementary evidence is provided by the survey X-ray photoelectron spectroscopy (XPS) spectrum (Figure S15 and Table S5), which shows comparable atomic ratios of S, Se, and P, suggesting homogeneous anion incorporation across the material. Based on the elemental composition obtained from XPS, the actual configurational entropy of NiFeZn-SSeP(OH)/NF was calculated to be 2.15*R*, with an anionic contribution of 1.31*R*, in close agreement with the theoretical value. Moreover, the total configurational entropy indicates that NiFeZn-SSeP(OH)/NF qualifies as a high-entropy material.

Further insights into the electronic modulation of metal centers were obtained from the high-resolution XPS spectra of Ni, Fe, and Zn (Figure 3g,h; Figure S16). Compared to the pristine LDH precursor, the multi-anion sample exhibits negative shifts in the binding energies of Ni, Fe and Zn, indicating partial decrease of their oxidation states as a result of multi-anion doping. Additionally, the appearance of characteristic Ni-S/Se/P and Fe-S/Se/P signals provides direct evidence of metal-anion coordination [62, 63]. Notably, the O 1s spectrum (Figure 3i) remains essentially unchanged in both peak positions and relative proportions of oxygen species, further suggesting that the observed shifts in metal oxidation states arise from the incorporated multi-anions, rather than altered metal–oxygen interaction. Furthermore, high-resolution S 2p, Se 3d, and P 2p spectra (Figure S17) exhibit M—S/M—Se/M—P doublets with only minor oxidized components, evidencing incorporation of S/Se/P into the single-phase LDH lattice and the resulting modulation of metal valence states. Taken together, these results indicate that the uniformly distributed S, Se, and P anions within the single-phase LDH lattice enable homogeneous regulation of the coordination environment and electronic structure of metal sites throughout the catalyst, which is expected to overcome the activity limitations of conventional phase-separated systems and deliver superior catalytic performance.

15214095, 2026, 20, Downloaded from https://advanced.onlinelibrary.wiley.com/doi/10.1002/adma.72791 by Yonghai Cao - South China University Of Technology , Wiley Online Library on [17/11/2026]. See the Terms and Conditions (https://onlinelibrary.wiley.com/terms-and-conditions) on Wiley Online Library for rules of use; OA articles are governed by the applicable Creative Commons License

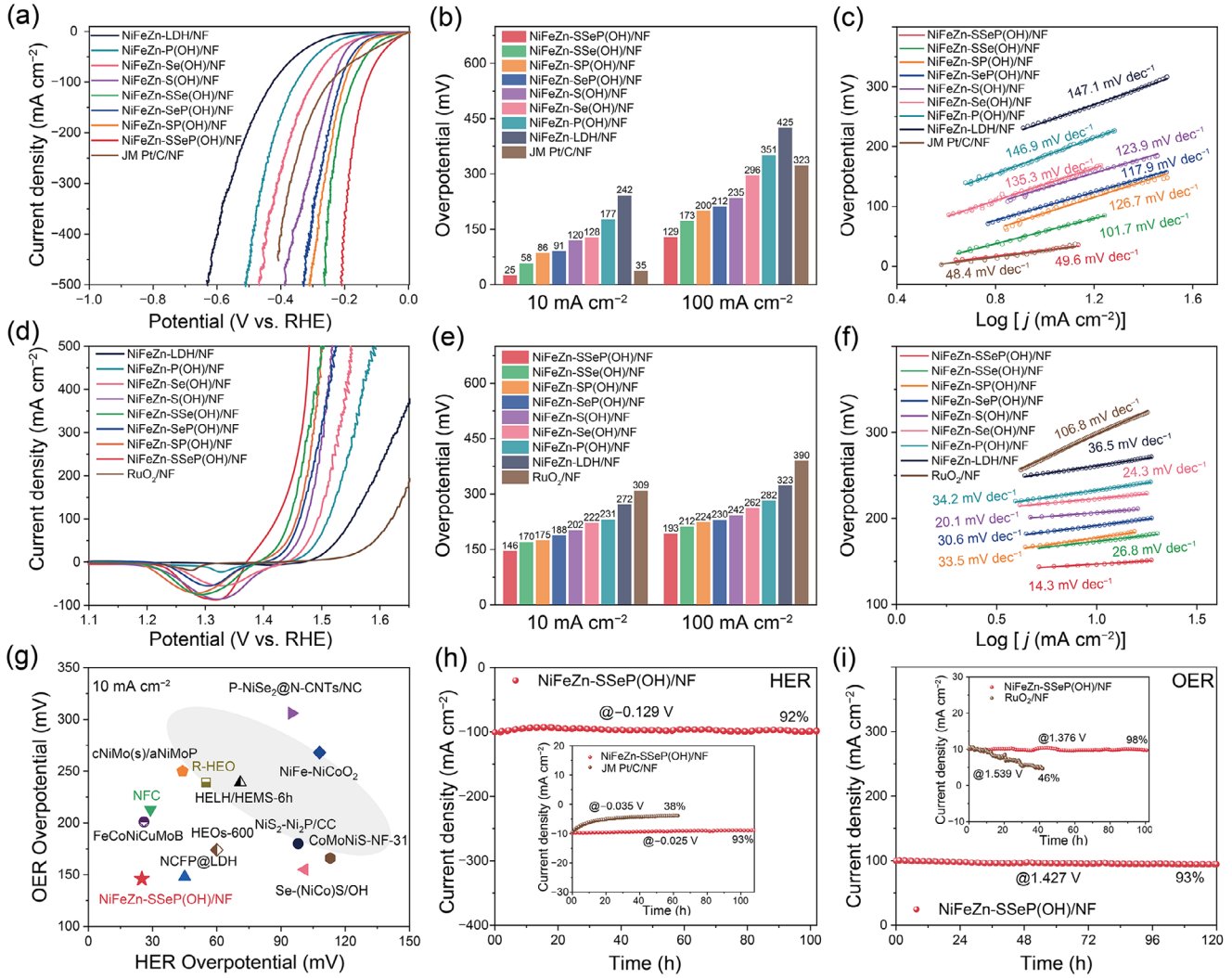

FIGURE 4 | Electrocatalytic performance of the NiFeZn-SSeP(OH)/NF multi-anion compound and contrast samples. (a) HER polarization curves, (b) overpotentials at current densities of 10 and 100 mA cm^{-2}, and (c) Tafel plots. (d) OER polarization curves, (e) overpotentials at 10 and 100 mA cm^{-2}, and (f) Tafel plots. (g) Comparison of HER and OER overpotentials with recently reported electrocatalysts. Chronoamperometry curve of NiFeZn-SSeP(OH)/NF for (h) HER and (i) OER stability testing; insets show comparisons with Pt/C/NF and RuO_2/NF, respectively. All measurements were conducted in 1.0 M KOH electrolyte.

2.3 | Electrocatalytic HER and OER Performance

The electrochemical performances of the multi-anion compounds were evaluated using a standard three-electrode setup in 1.0 M KOH solution. As shown in Figure 4a,b, linear sweep voltammetry (LSV) curves and the corresponding overpotential histograms reveal that NiFeZn-SSeP(OH)/NF delivers excellent HER performance, requiring only 25 mV and 129 mV to reach current densities of 10 and 100 mA cm^{-2}, respectively. These values surpass those of commercial Pt/C (45 mV at 10 mA cm^{-2}, 323 mV at 100 mA cm^{-2}) as well as all samples with lower anionic entropy. The Tafel slope of NiFeZn-SSeP(OH)/NF (49.6 mV dec^{-1}, Figure 4c) is comparable to that of Pt/C (48.4 mV dec^{-1}), and significantly lower than those of the lower-entropy counterparts, indicating accelerated HER kinetics. Electrochemical impedance spectroscopy (EIS) results (Figure S18) further show that NiFeZn-SSeP(OH)/NF possesses the lowest charge-transfer resistance (R_{ct} = 0.43 Ω), confirming its superior interfacial charge-transfer capability. A similar trend is observed for OER. As shown in Figure 4d–f, NiFeZn-SSeP(OH)/NF achieves ultralow overpotentials of 146 mV and 193 mV at 10 and 100 mA cm^{-2}, respectively, with a Tafel slope of only 14.3 mV dec^{-1}, outperforming all other samples. EIS data (Figure S19) again confirm the lowest R_{ct} (0.30 Ω) on NiFeZn- SSeP(OH)/NF under OER conditions, indicating its favorable OER kinetics.

To estimate the electrochemical active surface area (ECSA) and surface-normalized activity, the double-layer capacitance (C_{dl}) was measured via cyclic voltammetry (CV). As shown in Figure S20, NiFeZn-SSeP(OH)/NF shows a C_{dl} of 29.2 mF cm^{-2}, comparable to that of the LDH precursor NiFeZn-LDH/NF (27.1 mF cm^{-2}), further confirming the nanosheet morphology retention after anion substitution, as previously identified in the microscopy results. In contrast, samples with lower anionic entropy such as NiFeZn-Se(OH)/NF and NiFeZn-P(OH)/NF display markedly reduced C_{dl} values, indicative of disrupted

15214095, 2026, 20, Downloaded from https://advanced.onlinelibrary.wiley.com/doi/10.1002/adma.72791 by Yonghai Cao - South China University Of Technology , Wiley Online Library on [17/11/2026]. See the Terms and Conditions (https://onlinelibrary.wiley.com/terms-and-conditions) on Wiley Online Library for rules of use; OA articles are governed by the applicable Creative Commons License

morphologies and decreased accessible surface areas. Meanwhile, samples like NiFeZn-S(OH)/NF, NiFeZn-SSe(OH)/NF, and NiFeZn-SP(OH)/NF show elevated C_{dl} values, likely due to secondary structural growth on the nanosheet surfaces. Moreover, N_2 adsorption–desorption (Figure S21) shows BET specific surface areas of 31.41, 34.57, and 41.01 $m^2\ g^{-1}$ for NiFeZn-LDH, NiFeZn-SSeP(OH), and NiFeZn-SSe(OH), respectively, mirroring the trend of C_{dl}-derived ECSA. After ECSA-normalization (Figure S22), NiFeZn–SSeP(OH)/NF still exhibits the highest activity for both HER and OER, indicating that the superior performance arises from electronic structure modulation rather than surface area effects. More importantly, the turnover frequency (TOF) data (Figure S23) estimated based on the ECSA showed that NiFeZn-SSeP(OH)/NF exhibited the highest TOF values in both the hydrogen evolution reaction (HER) and the oxygen evolution reaction (OER), further illustrating the high intrinsic activity of the multi-anion compound. These electrochemical results indicate that the uniform incorporation of multiple anions effectively enhances the intrinsic activity for HER and OER, with the improvement arising from the synergy of these anions within an entropy-stabilized single-phase framework rather than simply adding different types of anions.

The influence of synthesis conditions for multi-anion compounds was also evaluated. As shown in Figure S24, varying the hydrothermal anion-exchange time reveals that the optimal HER and OER performance is achieved at the reaction time of 12 h. EIS analysis (Figure S25) confirms that this sample also features the lowest charge-transfer resistance. Moreover, with increasing synthesis time, the C_{dl} values (Figures S26 and S27) show an initial decrease followed by recovery to 29.2 mF cm^{-2} at 12 h, which is close to the initial value of the LDH precursor. Meanwhile, SEM (Figure S28) shows that all samples remain nanosheet-based, with partial nanosheet aggregation at 4–8 h. This phenomenon is consistent with the ECSA decrease inferred from Figure S21 and explains the activity drop, while longer times lead to re-dispersion and stabilization of both C_{dl} and activity. These results indicate that the high anionic entropy provides a thermodynamic driving force toward a structurally stable state during synthesis. Additional control experiments were conducted to evaluate the effects of substrate type (Figure S29), hydrothermal temperature (Figure S30), and anion concentration (Figure S31). In all cases, NiFeZn-SSeP(OH)/NF consistently exhibited the most favorable HER and OER activity. Notably, without multi-anion modification the activities of different cation frameworks such as $Ni(OH)_2$/NF, NiFe-LDH/NF, and NiFeZn-LDH/NF are low, whereas introducing multiple anions yields consistent and significant improvements (Figure S29). In addition, we constructed multi-anion compounds on other substrates including MoO_x, MoS_2, NiFeMo-LDH and NiCoMo-LDH (Figure S32), and the resulting multi-anionic materials showed significantly improved HER/OER bifunctional activity. These results indicate that the multi-anion effect can effectively enhance the activity of precursors with various types and amounts of metal cations, confirming the universality of multi-anion compounds.

When benchmarked against recently reported mixed-anion heterostructured catalysts and high-entropy oxides/hydroxides materials (Figure 4g and Table S6), NiFeZn-SSeP(OH)/NF ranks among the top-performing HER/OER bifunctional electrocatalysts. Finally, long-term electrochemical stability was assessed. As shown in Figure 4h,i, NiFeZn-SSeP(OH)/NF maintains stable HER and OER activity for over 100 h at a high current density of 100 mA cm^{-2}. In contrast, commercial Pt/C and RuO_2 suffer over 50% performance loss within just 40 h at 10 mA cm^{-2}, as shown in the insets. Moreover, ICP-OES (Table S3) of the NiFeZn-SSeP(OH)/NF after constant potential operation shows retention of S, Se, and P of at least 90 percent, indicating that the multi-anion framework possesses excellent stability. Furthermore, SEM and EDS elemental mapping results of NiFeZn-SSeP(OH)/NF after HER showed that the morphology of the nanosheets was maintained and the S, Se and P elements were still uniformly distributed (Figure S33). These comparisons underscore the effectiveness of the multi-anion design enabled by high anionic entropy, which yields a thermodynamically stable structure with uniform electronic modulation across all active sites. As a result, the NiFeZn-SSeP(OH)/NF catalyst overcomes the spatial and structural limitations of conventional phase-separated systems, offering outstanding bifunctional activity and long-term operational stability.

2.4 | Mechanistic Insights Into Multi-Anion-Induced Activity Enhancement

To elucidate the origin of the excellent catalytic activity exhibited by the multi-anion compounds, DFT calculations were performed, beginning with a study of the HER behavior. The structure model of single-phase NiFeZnSSePOH is shown in Figure 5a, where the S, Se, and P anions are uniformly distributed within the lattice. All models use the (001) crystal plane, which is most stable in LDHs, and has well-defined six-coordinate metal sites and regular atomic arrangement [64]. The differential charge density analysis (Figure 5b) indicates that, compared with the NiFeZnOH reference, the multi-anion doping in NiFeZnSSePOH leads to enhanced charge localization at metal active sites. We further compared the adsorption configurations of hydrogen atoms on Ni sites between the NiFeZnOH and NiFeZnSSePOH models (Figure 5c). The differential charge density profiles show clear overlap between the electron clouds of the doped anions and the adsorbed hydrogen (H*), suggesting that the presence of S, Se, and P modulates the local charge environment and contributes to favorable hydrogen adsorption energetics.

To explore the electronic structure in more detail, we calculated the projected density of states (PDOS) for a series of models with different anions (Figure 5d). The d-band centers of the Ni sites in all anion-regulated structures shift upward relative to the hydroxide model (−2.42 eV). Among them, single-anion doping with S or Se leads to minor shifts of the d-band center to −2.31 and −2.32 eV, respectively, whereas P doping alone induces an excessively positive shift to −1.51 eV. In contrast, the multi-anion NiFeZnSSePOH presents a more moderate d-band center of −1.94 eV. This appropriate modulation indicates that the electronic interaction between the metal centers and adsorbates is better balanced, which is favorable for enhancing catalytic performance.

The calculated Gibbs free energy of hydrogen adsorption (ΔG_H*) further supports this conclusion [65]. As shown in Figure 5e, NiFeZnSSePOH exhibits a ΔG_H* of −0.15 eV, which is significantly closer to the thermoneutral value (0 eV) than that of the

15214095, 2026, 20, Downloaded from https://advanced.onlinelibrary.wiley.com/doi/10.1002/adma.72791 by Yonghai Cao - South China University Of Technology , Wiley Online Library on [17/11/2026]. See the Terms and Conditions (https://onlinelibrary.wiley.com/terms-and-conditions) on Wiley Online Library for rules of use; OA articles are governed by the applicable Creative Commons License

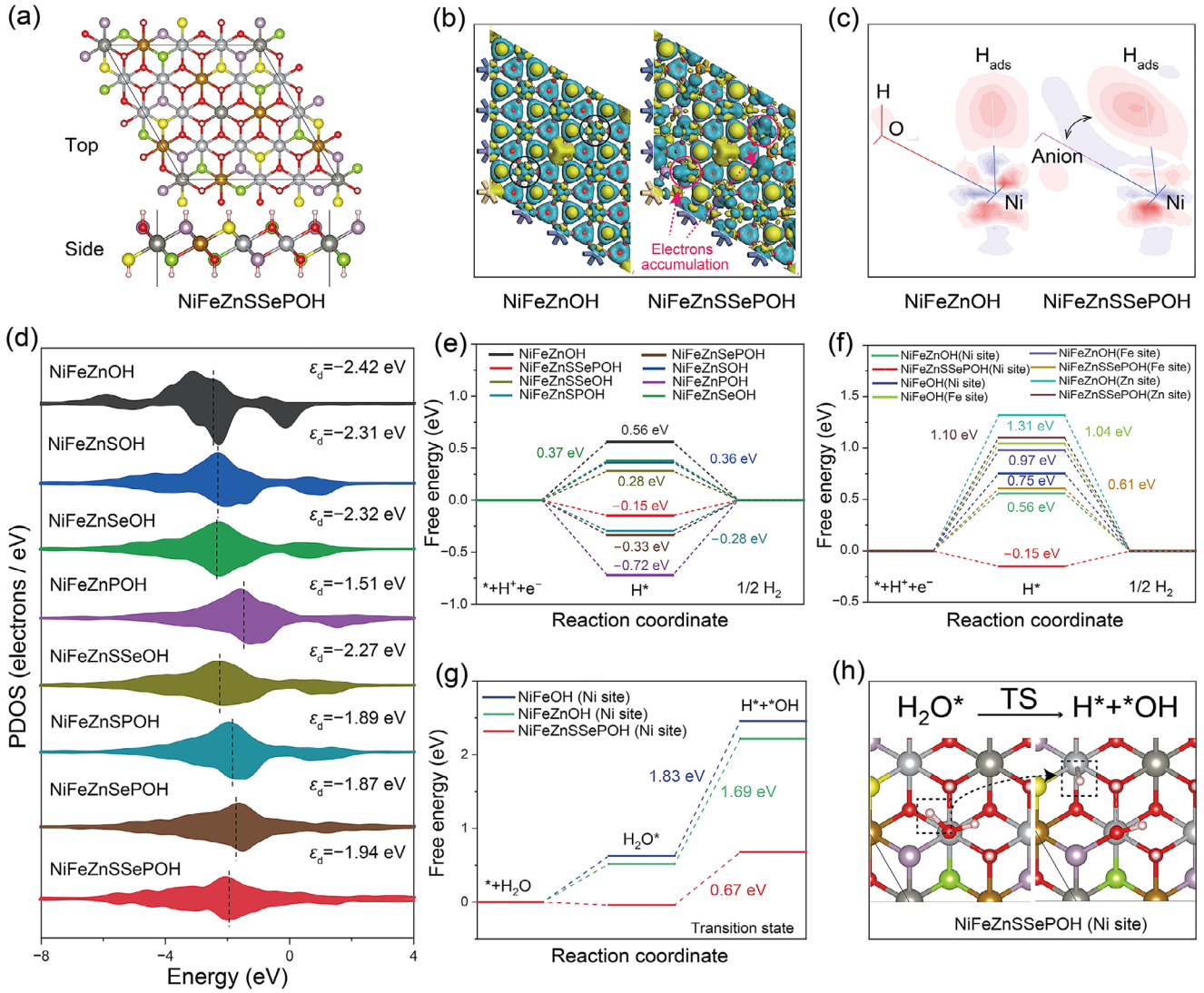

FIGURE 5 | (a) Structural model of NiFeZn-SSePOH. (b) Differential charge density maps of NiFeZnOH and NiFeZn-SSePOH. (c) Differential charge density maps of H adsorption at Ni sites in NiFeZnOH and NiFeZn-SSePOH. (d) Projected density of states (PDOS) of Ni atoms in multi-anion models. (e) Gibbs free energies of H adsorption (H*) at Ni sites in multi-anion models. (f) Gibbs free energies of H* at different metal sites in multi-anion models. (g) Water dissociation Gibbs free energies at Ni sites in NiFeOH, NiFeZnOH, and NiFeZn-SSePOH. (h) Schematic illustration of the water dissociation pathway at the Ni site in NiFeZn-SSePOH.

undoped NiFeZnOH (0.56 eV) and all other fewer-anion models. This result confirms that the multi-anion-doped single-phase structure effectively optimizes the HER activity of the Ni sites. Figure 5f provides a comparative analysis of ΔG_H* values for different metal sites, clearly demonstrating that the Ni site in NiFeZnSSePOH offers the most favorable hydrogen adsorption behavior. Considering that alkaline HER involves an initial water dissociation step, we also calculated the energy barriers of water dissociation at the Ni sites for NiFeOH, NiFeZnOH, and NiFeZnSSePOH models. As illustrated in Figure 5g, energy barriers of Ni sites for water dissociation are substantially reduced in the NiFeZnSSePOH system (0.67 eV), compared to 1.83 eV for NiFeOH and 1.69 eV for NiFeZnOH. These results highlight the significant improvement in reaction kinetics enabled by multi-anion doping. The corresponding reaction pathway of water dissociation at the Ni site is schematically shown in Figure 5h. Overall, the DFT results reveal that the single-phase multi-anion structure not only optimizes the hydrogen adsorption free energy but also significantly lowers the water dissociation energy barrier. The theoretical calculations are in strong agreement with the experimental results, providing a consistent mechanism that explains the observed excellent catalytic performance for HER.

Considering the potential oxidation of the catalysts during OER, structural characterization was first performed on the post-reaction samples, followed by DFT calculations to investigate the OER catalytic mechanism of the multi-anion compounds. As shown in the SEM image in Figure 6a, NiFeZn-SSeP(OH)/NF retains its typical nanosheet morphology even after the high oxidation potential process of OER. The corresponding EDS mapping (Figure S34) confirms that elemental distribution remains uniform after the OER. Furthermore, HRTEM analysis (Figure 6b) shows the formation of a ~3–5 nm thick partially oxidized layer along the nanosheet edges after OER, with a lattice spacing of 0.286 nm corresponding to the (011) plane of NiOOH, consistent with the XRD results shown in

15214095, 2026, 20, Downloaded from https://advanced.onlinelibrary.wiley.com/doi/10.1002/adma.72791 by Yonghai Cao - South China University Of Technology , Wiley Online Library on [17/11/2026]. See the Terms and Conditions (https://onlinelibrary.wiley.com/terms-and-conditions) on Wiley Online Library for rules of use; OA articles are governed by the applicable Creative Commons License

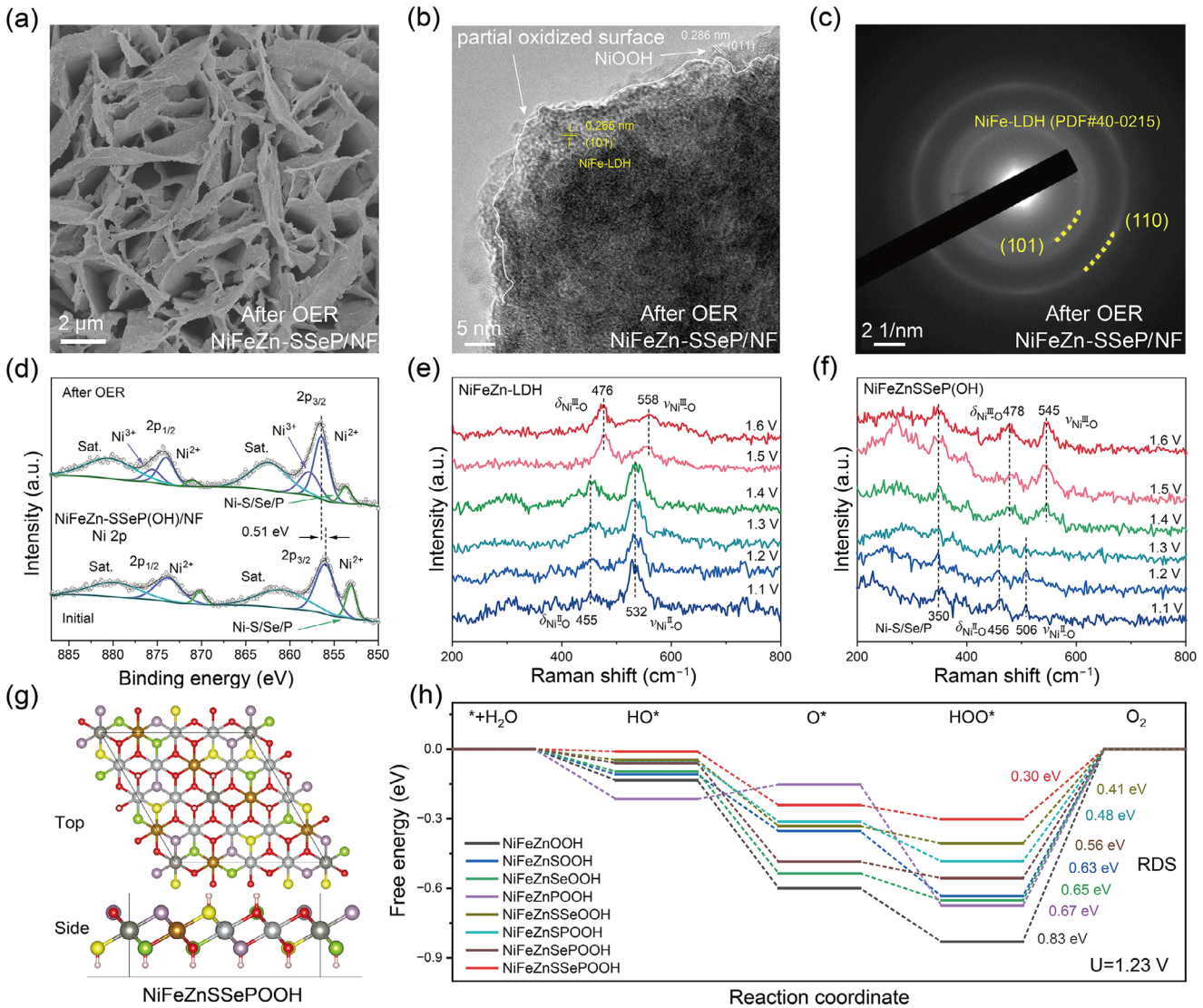

FIGURE 6 | (a) SEM, (b) HRTEM, and (c) SAED images of NiFeZn-SSeP(OH)/NF after OER. (d) High-resolution Ni 2p XPS spectra of NiFeZn-SSeP(OH)/NF before and after OER. Raman spectra of (e) NiFeZn-LDH and (f) NiFeZn-SSeP(OH)/NF collected at different applied potentials. (g) Structural model of NiFeZnSSePOOH. (h) Free energy diagrams of the OER process on multi-anion models.

Figure S35 [66]. In addition, the SAED pattern (Figure 6c) exhibits diffraction rings consistent with those before OER, with only a slight decrease in crystallinity, indicating that the crystalline framework of the multi-anion compound remains intact under high OER potentials. Notably, TEM-based EDS elemental mapping (Figure S36) reveals that the doped anions remain uniformly distributed across both the surface and edge regions after OER, with no observable aggregation. These results confirm that the multi-anion compound retains a homogeneously distributed anionic configuration even after long-term OER operation. XPS further elucidates the changes in the electronic structure. The high-resolution Ni 2p spectrum (Figure 6d) exhibits a positive shift of 0.51 eV in the Ni^{2+} peak, indicating an increase in the Ni oxidation state. Concurrently, the O 1s spectrum (Figure S37) shows a negative shift in the M—OH and M—O components and a significant enlargement of the M—O peak area, suggesting the formation of metal oxyhydroxide during the OER process [67]. The phase transition behavior during OER was further analyzed by Raman spectroscopy (Figure 6e,f). Upon increasing the applied potential, both the δ(Ni—O) and the ν(Ni—O) bands shift toward higher wavenumbers, reflecting the oxidation of Ni(II) to Ni(III) species. For NiFeZn-SSeP(OH), the onset potential of this transition is 1.4 V, lower than that observed for NiFeZn-LDH (1.5 V), suggesting that the multi-anion incorporation favors the generation of high-valence active sites for OER [68]. The accelerated reconstruction of the multi-anion compound into an OER-active oxyhydroxide under OER potentials, which is attributed to the reduced initial Ni valence state due to the introduction of multi-anions [69, 70]. Moreover, the Raman spectra of NiFeZn-SSeP(OH) show no observable change in the metal–S/Se/P coordination peak at 350 cm^{-1} during the OER process, indicating the structural stability of the multi-anion coordination environment. According to these results, the NiFeZn-SSeP(OH) catalyst can be identified as a multi-anion-doped oxyhydroxide under OER conditions.

Based on post-OER structural characterizations, we constructed a NiFeZnSSePOOH model (Figure 6g; Figure S38) that is consistent

15214095, 2026, 20, Downloaded from https://advanced.onlinelibrary.wiley.com/doi/10.1002/adma.72791 by Yonghai Cao - South China University Of Technology , Wiley Online Library on [17/11/2026]. See the Terms and Conditions (https://onlinelibrary.wiley.com/terms-and-conditions) on Wiley Online Library for rules of use; OA articles are governed by the applicable Creative Commons License

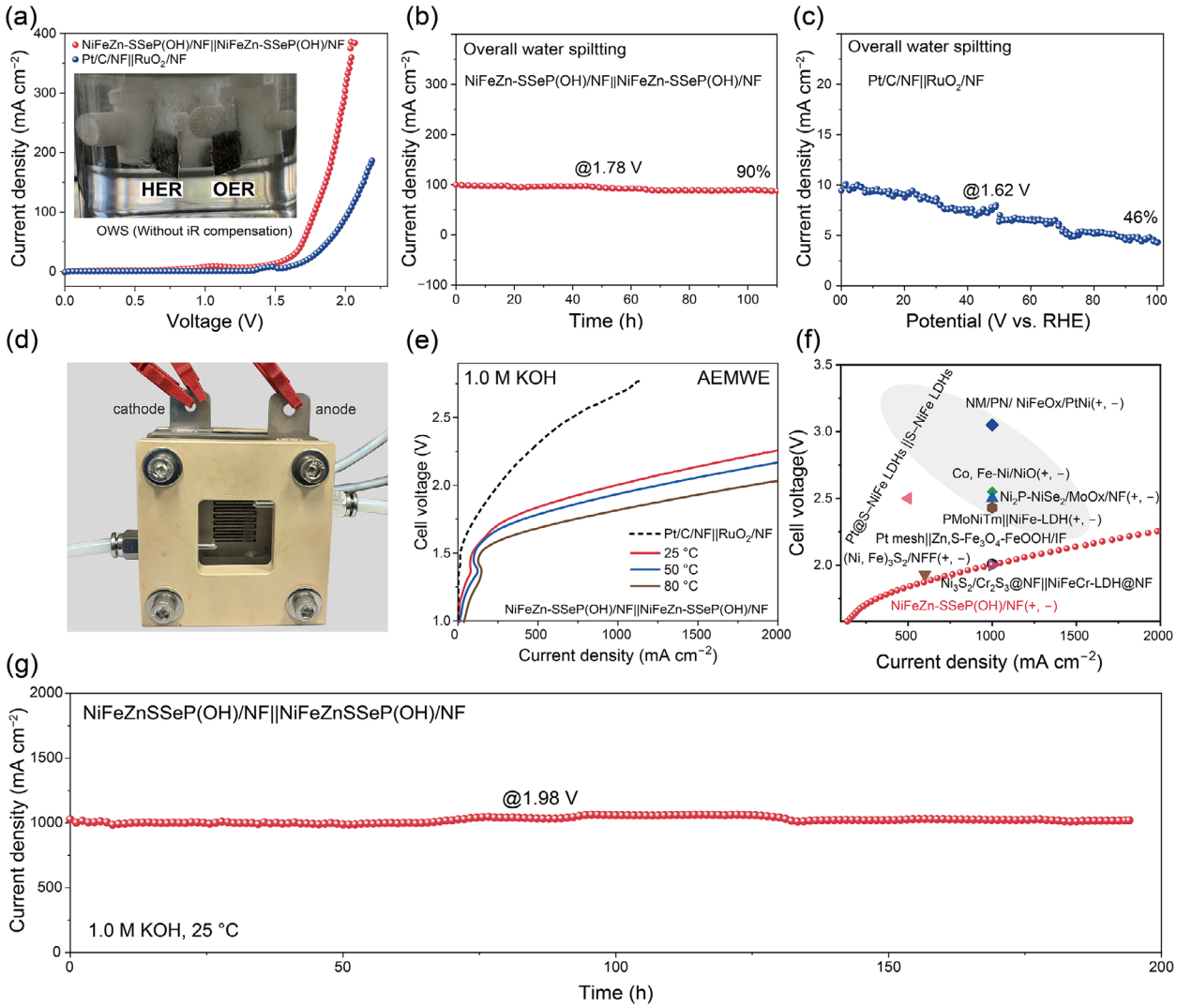

FIGURE 7 | (a) Polarization curve for overall water splitting using NiFeZn-SSeP(OH)/NF||NiFeZn-SSeP(OH)/NF. Chronoamperometry stability curves of (b) NiFeZn-SSeP(OH)/NF||NiFeZn-SSeP(OH)/NF and (c) Pt/C/NF||RuO_2/NF. (d) Photograph of the assembled AEM water electrolyzer. (e) Polarization curves of the AEM water electrolyzer using NiFeZn-SSeP(OH)/NF||NiFeZn-SSeP(OH)/NF and Pt/C/NF||RuO_2/NF. (f) Comparison of AEM electrolyzer performance in this work with recently reported systems. (g) Long-term chronoamperometry stability curve of NiFeZn-SSeP(OH)/NF||NiFeZn-SSeP(OH)/NF at 1.98 V.

with the measurements, employing a Ni(FeZn)OOH-type slab with OOH-terminated surfaces, the measured Ni/Fe/Zn stoichiometry, and a near-random subsurface S/Se/P distribution in line with the XRD, spectroscopic, and compositional analyses. Considering the recognized catalytic superiority of Ni sites, we computed the Gibbs free energy changes for the OER steps at Ni active centers in models with different anion diversity. By calculating the free energy of each elementary step (Figure S39), we identified the rate-determining step (RDS) and corresponding limiting potential for each system. As shown in the free energy step diagram in Figure 6h, the desorption of HOO* is the RDS for all models in OER process. Among them, NiFeZnSSePOOH exhibits the lowest energy barrier of only 0.30 eV, reflecting highly favorable reaction kinetics. This theoretical prediction is consistent with the experimental results, including a low OER overpotential (146 mV at 10 mA cm^{-2}) and a small Tafel slope (14.3 mV dec^{-1}). Collectively, these results indicate that the multi-anion-doped oxyhydroxide structure formed during OER synergistically modulates the electronic structure of Ni sites and effectively lowers the reaction energy barriers, thereby enhancing the intrinsic OER activity.

2.5 | Application in Overall Water Splitting Devices

Finally, the overall water splitting performance of the NiFeZn-SSeP(OH)/NF catalyst was evaluated. In a two-electrode electrolysis cell, the NiFeZn-SSeP(OH)/NF||NiFeZn-SSeP(OH)/NF configuration requires only 1.78 V to achieve a current density of 100 mA cm^{-2}, significantly outperforming the commercial Pt/C/NF||RuO_2/NF system (Figure 7a). In the long-term durability testing (Figure 7b), the NiFeZn-SSeP(OH)/NF-based system still retained 90% of its initial activity after 100 h of continuous operation at 100 mA cm^{-2}. By contrast, the Pt/C/NF||RuO_2/NF counterpart (Figure 7c) exhibited a 54% decline in performance

15214095, 2026, 20, Downloaded from https://advanced.onlinelibrary.wiley.com/doi/10.1002/adma.72791 by Yonghai Cao - South China University Of Technology , Wiley Online Library on [17/11/2026]. See the Terms and Conditions (https://onlinelibrary.wiley.com/terms-and-conditions) on Wiley Online Library for rules of use; OA articles are governed by the applicable Creative Commons License

under a much lower current density of 10 mA cm^{-2}, highlighting the superior stability of the multi-anion catalyst. To further assess its practical applicability, an anion exchange membrane (AEM) water electrolyzer was assembled using NiFeZn-SSeP(OH)/NF as both the anode and cathode (Figure 7d). As shown in Figure 7e, this electrolyzer delivers an industrial-level current density of 1,000 mA cm^{-2} with cell voltages of 1.98 V at 25°C, 1.92 V at 50°C, and 1.81 V at 80°C, substantially lower than the 2.69 V at 25°C needed by the Pt/C/NF||RuO_2/NF system. Moreover, this performance is superior to other recently reported AEM water electrolyzers, as shown in Figure 7f and Table S7. Notably, the assembled electrolyzer maintained a steady output of 1,000 mA cm^{-2} with virtually no degradation after 200 h of continuous operation at 1.98 V (Figure 7g), fully demonstrating its strong potential for industrial-scale hydrogen production.

3 | Conclusions

In conclusion, we have developed a new entropy-driven strategy to construct single-phase multi-anion compounds through anion configurational entropy engineering. Using a model system containing hydroxide, sulfur, selenium and phosphorus anions, we demonstrated that high anionic configurational entropy thermodynamically stabilizes the state of uniform anion mixing, as evidenced by both experimental and theoretical analyses. This multi-anion configuration enables precise regulation of the electronic structure across all metal active sites. As a result, the obtained NiFeZn-SSeP(OH)/NF catalyst exhibits exceptional bifunctional electrocatalytic performance, with low overpotentials of 25 mV for HER and 146 mV for OER at 10 mA cm^{-2}, along with excellent reaction kinetics and structural stability. When employed in a practical AEM water electrolyzer, the catalyst achieves 1,000 mA cm^{-2} at 1.98 V and maintains continuous operation for over 200 h at 25 °C. Mechanistic investigations further reveal that the co-substitution of S, Se, and P modulates the Ni valence state and adsorption energetics during HER and OER, while maintaining structural uniformity even under high anodic potentials. These findings establish an effective entropy-guided design principle for tailoring multi-anionic coordination environments, introducing multi-anion compounds as a new member of the high-entropy material family, and providing a generalizable route to high-performance, durable electrocatalysts for next-generation energy conversion technologies.

Acknowledgements

This work was financially supported by National Natural Science Foundation of China (No. 22209049) and Natural Science Foundation of Guangdong Province (Nos. 2023A1515012804 and 2025A1515010003).

Funding

This work is financially supported by National Natural Science Foundation of China (No. 22209049) and Natural Science Foundation of Guangdong Province (Nos. 2023A1515012804 and 2025A1515010003).

Conflicts of Interest

None of the authors have a conflict of interest to disclose.

Data Availability Statement

The data that support the findings of this study are available from the corresponding author upon reasonable request.

References

1. S. W. Boettcher, "Introduction to Green Hydrogen," *Chemical Reviews* 124 (2024): 13095–13098, https://doi.org/10.1021/acs.chemrev.4c00787.

2. C. Gunathilake, I. Soliman, D. Panthi, et al., "A Comprehensive Review on Hydrogen Production, Storage, and Applications," *Chemical Society Reviews* 53 (2024): 10900–10969, https://doi.org/10.1039/D3CS00731F.

3. S. S. Kumar and H. Lim, "An Overview of Water Electrolysis Technologies for Green Hydrogen Production," *Energy Reports* 8 (2022): 13793–13813, https://doi.org/10.1016/j.egyr.2022.10.127.

4. X. Gao, Y. Chen, Y. Wang, et al., "Next-Generation Green Hydrogen: Progress and Perspective From Electricity, Catalyst to Electrolyte in Electrocatalytic Water Splitting," *Nano-Micro Letters* 16 (2024): 237, https://doi.org/10.1007/s40820-024-01424-2.

5. Z. Li, G. Lin, L. Wang, et al., "Seed-Assisted Formation of NiFe Anode Catalysts for Anion Exchange Membrane Water Electrolysis at Industrial-Scale Current Density," *Nature Catalysis* 7 (2024): 944–952, https://doi.org/10.1038/s41929-024-01209-1.

6. K. Ham, S. Bae, and J. Lee, "Classification and Technical Target of Water Electrolysis for Hydrogen Production," *Journal of Energy Chemistry* 95 (2024): 554–576, https://doi.org/10.1016/j.jechem.2024.04.003.

7. Z.-Y. Yu, Y. Duan, X.-Y. Feng, X. Yu, M.-R. Gao, and S.-H. Yu, "Clean and Affordable Hydrogen Fuel From Alkaline Water Splitting: Past, Recent Progress, and Future Prospects," *Advanced Materials* 33 (2021): 2007100, https://doi.org/10.1002/adma.202007100.

8. L. Quan, H. Jiang, G. L. Mei, Y. J. Sun, and B. You, "Bifunctional Electrocatalysts for Overall and Hybrid Water Splitting," *Chemical Reviews* 124 (2024): 3694–3812, https://doi.org/10.1021/acs.chemrev.3c00332.

9. W. Li, Y. Liu, A. Azam, et al., "Unlocking Efficiency: Minimizing Energy Loss in Electrocatalysts for Water Splitting," *Advanced Materials* 36 (2024): 2404658, https://doi.org/10.1002/adma.202404658.

10. G. Gao, Z. Sun, X. Chen, et al., "Recent Advances in Hydrogen Production Coupled With Alternative Oxidation Reactions," *Coordination Chemistry Reviews* 509 (2024): 215777, https://doi.org/10.1016/j.ccr.2024.215777.

11. N. K. Oh, J. Seo, S. Lee, et al., "Highly Efficient and Robust Noble-Metal Free Bifunctional Water Electrolysis Catalyst Achieved via Complementary Charge Transfer," *Nature Communications* 12 (2021): 4606, https://doi.org/10.1038/s41467-021-24829-8.

12. L. Chen, X. Dong, Y. Wang, and Y. Xia, "Separating Hydrogen and Oxygen Evolution in Alkaline Water Electrolysis Using Nickel Hydroxide," *Nature Communications* 7 (2016): 11741, https://doi.org/10.1038/ncomms11741.

13. S. Liu, Y. Wei, M. Wang, and Y. Shen, "The Future of Alkaline Water Splitting From the Perspective of Electrocatalysts-Seizing Today's Opportunities," *Coordination Chemistry Reviews* 522 (2025): 216190, https://doi.org/10.1016/j.ccr.2024.216190.

14. M. Sun, R. Ge, S. Li, et al., "The Component-Activity Interrelationship of Cobalt-Based Bifunctional Electrocatalysts for Overall Water Splitting: Strategies and Performance," *Journal of Energy Chemistry* 91 (2024): 453–474, https://doi.org/10.1016/j.jechem.2023.12.033.

15. Y. Sun, J. Dai, H. Lv, et al., "Superhydrophilic V-Doped CoP Nanoparticles@Cu_3P Nanotubes With Vacancy and Interface Engineering for Synergistically Enhanced Electrocatalytic Overall Water Splitting," *Advanced Functional Materials* 35 (2025): 2505867, https://doi.org/10.1002/adfm.202505867.

16. Y. Wang, J. Wang, J. Xu, et al., "Fullerene-Buffered Electron Shuttle of Ru/RuO_2 With Switchable Active Sites Enables Robust and Efficient Bifunctional Alkaline Water Electrolysis," *Angewandte Chemie*

15214095, 2026, 20, Downloaded from https://advanced.onlinelibrary.wiley.com/doi/10.1002/adma.72791 by Yonghai Cao - South China University Of Technology , Wiley Online Library on [17/11/2026]. See the Terms and Conditions (https://onlinelibrary.wiley.com/terms-and-conditions) on Wiley Online Library for rules of use; OA articles are governed by the applicable Creative Commons License

International Edition 64 (2025): 202503608, https://doi.org/10.1002/anie.202503608.

17. Y. Pan, K. Sun, S. Liu, et al., "Core–Shell ZIF-8@ZIF-67-Derived CoP Nanoparticle-Embedded N-Doped Carbon Nanotube Hollow Polyhedron for Efficient Overall Water Splitting," *Journal of the American Chemical Society* 140 (2018): 2610–2618, https://doi.org/10.1021/jacs.7b12420.

18. J. Wang, F. Xu, H. Jin, Y. Chen, and Y. Wang, "Non-Noble Metal-based Carbon Composites in Hydrogen Evolution Reaction: Fundamentals to Applications," *Advanced Materials* 29 (2017): 1605838, https://doi.org/10.1002/adma.201605838.

19. Y. Tsubonouchi, Z. N. Zahran, D. Chandra, N. Hoshino, and M. Yagi, "Prominent Development of Ni-Based Oxygen-Evolving Electrocatalysts for Water Splitting," *Catalysis Science & Technology* 14 (2024): 3287–3319, https://doi.org/10.1039/D4CY00066H.

20. M. Wang, Y. Wang, S. S. Mao, and S. Shen, "Transition-Metal Alloy Electrocatalysts With Active Sites Modulated by Metal-Carbide Heterophases for Efficient Oxygen Evolution," *Nano Energy* 88 (2021): 106216, https://doi.org/10.1016/j.nanoen.2021.106216.

21. S. Bulakhe, N. Shinde, J.-S. Kim, R. S. Mane, and R. Deokate, "Recent Advances in Non-Precious Ni-Based Promising Catalysts for Water Splitting Application," *International Journal of Energy Research* 46 (2022): 17829–17847, https://doi.org/10.1002/er.8458.

22. C. Chen, P.-Y. Olu, R. Fan, and M. Shen, "Review of Ni-Based Materials for Industrial Alkaline Hydrogen Production," *Chemsuschem* 18 (2025): 202401415, https://doi.org/10.1002/cssc.202401415.

23. T. Liu, A. Li, C. Wang, W. Zhou, S. Liu, and L. Guo, "Interfacial Electron Transfer of Ni_2P–NiP_2 Polymorphs Inducing Enhanced Electrochemical Properties," *Advanced Materials* 30 (2018): 1803590, https://doi.org/10.1002/adma.201803590.

24. J. Zhu, M. Sun, S. Liu, X. Liu, K. Hu, and L. Wang, "Study of Active Sites on Se-MnS/NiS Heterojunctions as Highly Efficient Bifunctional Electrocatalysts for Overall Water Splitting," *Journal of Materials Chemistry A* 7 (2019): 26975–26983, https://doi.org/10.1039/C9TA10860B.

25. J. Zhou, P. Li, X. Xia, et al., "Precisely Tailoring the D-Band Center of Nickel Sulfide for Boosting Overall Water Splitting," *Applied Catalysis B: Environment and Energy* 359 (2024): 124461, https://doi.org/10.1016/j.apcatb.2024.124461.

26. Y. Liu, T. Sakthivel, F. Hu, et al., "Enhancing the d/p-Band Center Proximity With Amorphous-Crystalline Interface Coupling for Boosted pH-Robust Water Electrolysis," *Advanced Energy Materials* 13 (2023): 2203797, https://doi.org/10.1002/aenm.202203797.

27. Y. Jiang, S. Gao, X. Liu, et al., "Recent Achievements in Selenium-Based Transition Metal Electrocatalysts for pH-Universal Water Splitting," *Nano Research* 17 (2024): 5763–5785, https://doi.org/10.1007/s12274-024-6485-9.

28. J. Ren, Z. Hu, C. Chen, Y. Liu, and Z. Yuan, "Integrated Ni_2P Nanosheet Arrays on Three-Dimensional Ni Foam for Highly Efficient Water Reduction and Oxidation," *Journal of Energy Chemistry* 26 (2017): 1196–1202, https://doi.org/10.1016/j.jechem.2017.07.016.

29. P. Liu and J. A. Rodriguez, "Catalysts for Hydrogen Evolution From the [NiFe] Hydrogenase to the Ni_2P(001) Surface: the Importance of Ensemble Effect," *Journal of the American Chemical Society* 127 (2005): 14871–14878, https://doi.org/10.1021/ja0540019.

30. E. J. Popczun, J. R. McKone, C. G. Read, et al., "Nanostructured Nickel Phosphide as an Electrocatalyst for the Hydrogen Evolution Reaction," *Journal of the American Chemical Society* 135 (2013): 9267–9270, https://doi.org/10.1021/ja403440e.

31. H. Meng, W. Zhang, Z. Ma, et al., "Self-Supported Ternary Ni–S–Se Nanorod Arrays as Highly Active Electrocatalyst for Hydrogen Generation in Both Acidic and Basic Media: Experimental Investigation and DFT Calculation," *ACS Applied Materials & Interfaces* 10 (2018): 2430–2441, https://doi.org/10.1021/acsami.7b14506.

32. Z. Dai, H. Geng, J. Wang, et al., "Hexagonal-Phase Cobalt Monophosphosulfide for Highly Efficient Overall Water Splitting," *ACS Nano* 11 (2017): 11031–11040, https://doi.org/10.1021/acsnano.7b05050.

33. J. Sun, X. Hu, Z. Huang, et al., "Atomically Thin Defect-rich Ni-Se-S Hybrid Nanosheets as Hydrogen Evolution Reaction Electrocatalysts," *Nano Research* 13 (2020): 2056–2062, https://doi.org/10.1007/s12274-020-2807-8.

34. Q. Fu, L. Yang, W. Wang, et al., "Synthesis and Enhanced Electrochemical Catalytic Performance of Monolayer $WS_{2(1-x)}Se_{2x}$ With a Tunable Band Gap," *Advanced Materials* 27 (2015): 4732–4738, https://doi.org/10.1002/adma.201500368.

35. Y. Liu, Q. Feng, W. Liu, et al., "Boosting Interfacial Charge Transfer for Alkaline Hydrogen Evolution via Rational Interior Se Modification," *Nano Energy* 81 (2021): 105641, https://doi.org/10.1016/j.nanoen.2020.105641.

36. N. Shaikh, I. Mukhopadhyay, and A. Ray, "Heterointerfaces of Nickel Sulphides and Selenides on Ni-Foam as Efficient Bifunctional Electrocatalysts in Acidic Environments," *Journal of Materials Chemistry A* 10 (2022): 12733–12746, https://doi.org/10.1039/D2TA01630C.

37. D. Xu, X. Li, Z. Liu, et al., "Crystal Field Stabilization Energy Asymmetrically Constructed Built-in Electric Fields for Efficient Water Cracking," *Small* 21 (2025): 2502250, https://doi.org/10.1002/smll.202502250.

38. C.-X. Zhao, B.-Q. Li, M. Zhao, et al., "Precise Anionic Regulation of NiFe Hydroxysulfide Assisted by Electrochemical Reactions for Efficient Electrocatalysis," *Energy & Environmental Science* 13 (2020): 1711–1716, https://doi.org/10.1039/C9EE03573G.

39. B.-Q. Li, S.-Y. Zhang, C. Tang, X. Cui, and Q. Zhang, "Anionic Regulated NiFe (Oxy)Sulfide Electrocatalysts for Water Oxidation," *Small* 13 (2017): 1700610, https://doi.org/10.1002/smll.201700610.

40. N. Attarzadeh, D. Das, S. N. Chintalapalle, S. Tan, V. Shutthanandan, and C. V. Ramana, "Nature-Inspired Design of Nano-Architecture-Aligned Ni_5P_4-Ni_2P/NiS Arrays for Enhanced Electrocatalytic Activity of Hydrogen Evolution Reaction (HER)," *ACS Applied Materials & Interfaces* 15 (2023): 22036–22050, https://doi.org/10.1021/acsami.3c00781.

41. Y. Huang, Y. Pan, X. Huang, J. Zhao, and X. Wang, "Porous NiS@Ni_2P Nanoframe as a Multi-Functional Catalyst for Enhanced Oxygen Evolution and Urea Oxidation Reactions," *Journal of Industrial and Engineering Chemistry* 118 (2023): 239–246, https://doi.org/10.1016/j.jiec.2022.11.009.

42. R.-Z. Zhang, F. Gucci, H. Zhu, K. Chen, and M. J. Reece, "Data-Driven Design of Ecofriendly Thermoelectric High-Entropy Sulfides," *Inorganic Chemistry* 57 (2018): 13027–13033, https://doi.org/10.1021/acs.inorgchem.8b02379.

43. C. M. Rost, E. Sachet, T. Borman, et al., "Entropy-Stabilized Oxides," *Nature Communications* 6 (2015): 8485, https://doi.org/10.1038/ncomms9485.

44. R.-Z. Zhang and M. J. Reece, "Review of High Entropy Ceramics: Design, Synthesis, Structure and Properties," *Journal of Materials Chemistry A* 7 (2019): 22148–22162, https://doi.org/10.1039/C9TA05698J.

45. D. Liu, P. Guo, H. Pan, and R. Wu, "Emerging High-Entropy Compounds for Electrochemical Energy Storage and Conversion," *Progress in Materials Science* 145 (2024): 101300, https://doi.org/10.1016/j.pmatsci.2024.101300.

46. D. Liu, P. Guo, X. Yan, Y. He, and R. Wu, "Manipulating the Configuration Entropy of Layered Hydroxides Toward Efficient Oxygen Evolution Reaction for Anion Exchange Membrane Electrolyzer," *Materials Today* 80 (2024): 101–112, https://doi.org/10.1016/j.mattod.2024.08.008.

47. D. Liu, P. Guo, Q. Wang, et al., "Local Proton-Mediated Synthesis of a High-Entropy Borate Library," *Advanced Materials* 37 (2025): 2414067, https://doi.org/10.1002/adma.202414067.

48. C.-X. Zhao, H.-F. Wang, B.-Q. Li, and Q. Zhang, "Multianion Transition Metal Compounds: Synthesis, Regulation, and Electrocatalytic Applications," *Accounts of Materials Research* 2 (2021): 1082–1092, https://doi.org/10.1021/accountsmr.1c00136.

15214095, 2026, 20, Downloaded from https://advanced.onlinelibrary.wiley.com/doi/10.1002/adma.72791 by Yonghai Cao - South China University Of Technology , Wiley Online Library on [17/11/2026]. See the Terms and Conditions (https://onlinelibrary.wiley.com/terms-and-conditions) on Wiley Online Library for rules of use; OA articles are governed by the applicable Creative Commons License

49. J. Zhang, X. Liu, Y. Ji, et al., "Atomic-Thick Metastable Phase RhMo Nanosheets for Hydrogen Oxidation Catalysis," *Nature Communications* 14 (2023): 1761, https://doi.org/10.1038/s41467-023-37406-y.

50. B.-K. Li, L.-P. Fu, H.-Z. Gu, A. Huang, and S. Yang, "Novel Entropy-Stabilized Spinel Materials and Their Potential Application in High-Temperature Industry: $[(Mg_xZn_{(1-x)/2}Cu_{(1-x)/2})(Al_{0.9}Fe_{0.1})_2O_4]$ $(x = 0.5, 0.6, 0.7,$ and $0.8)$," *Rare Metals* 44 (2025): 5844–5858, https://doi.org/10.1007/s12598-025-03265-3.

51. H. Cao, Q. Wang, Z. Zhang, et al., "Engineering Single-Atom Electrocatalysts for Enhancing Kinetics of Acidic Volmer Reaction," *Journal of the American Chemical Society* 145 (2023): 13038–13047, https://doi.org/10.1021/jacs.2c13418.

52. S. R. Khaladkar, O. Maurya, G. Gund, et al., "Extrinsic Pseudocapacitive NiSe/rGO/G-C_3N_4 Nanocomposite for High-Performance Hybrid Supercapacitors," *ACS Applied Materials & Interfaces* 16 (2024): 11408–11420, https://doi.org/10.1021/acsami.3c16010.

53. C. Huang, Q. Zhou, D. Duan, et al., "The Rapid Self-Reconstruction of Fe-Modified Ni Hydroxysulfide for Efficient and Stable Large-Current-Density Water/Seawater Oxidation," *Energy & Environmental Science* 15 (2022): 4647–4658, https://doi.org/10.1039/D2EE01478E.

54. Z. Cheng, H. Abernathy, and M. Liu, "Raman Spectroscopy of Nickel Sulfide Ni_3S_2," *The Journal of Physical Chemistry C* 111 (2007): 17997–18000, https://doi.org/10.1021/jp0770209.

55. X. Ding, D. Liu, A. wang, et al., "In Situ Reconstruction of Nickel Selenide for Enhanced Hydrogen Evolution Reaction," *Advanced Functional Materials* 36 (2025): 21566, https://doi.org/10.1002/adfm.202521566.

56. X. Yu, Z.-Y. Yu, X.-L. Zhang, et al., ""Superaerophobic" Nickel Phosphide Nanoarray Catalyst for Efficient Hydrogen Evolution at Ultrahigh Current Densities," *Journal of the American Chemical Society* 141 (2019): 7537–7543, https://doi.org/10.1021/jacs.9b02527.

57. W. Li, Y. Ding, Y. Zhao, et al., "Zwitterion-Modified NiFe OER Catalyst Achieving Ultrastable Anion Exchange Membrane Water Electrolysis via Dynamic Alkaline Microenvironment Engineering," *Angewandte Chemie International Edition* 64 (2025): 202505924, https://doi.org/10.1002/anie.202505924.

58. L. Peng, N. Yang, Y. Yang, et al., "Atomic Cation-Vacancy Engineering of NiFe-Layered Double Hydroxides for Improved Activity and Stability towards the Oxygen Evolution Reaction," *Angewandte Chemie International Edition* 60 (2021): 24612–24619, https://doi.org/10.1002/anie.202109938.

59. D. D. Alemayehu, M.-C. Tsai, M.-H. Tsai, et al., "Heterogeneous Interfaces of Ni_3Se_4 Nanoclusters Decorated on a Ni_3N Surface Enhance Efficient and Durable Hydrogen Evolution Reactions in Alkaline Electrolyte," *Journal of the American Chemical Society* 147 (2025): 16047–16059, https://doi.org/10.1021/jacs.4c17747.

60. K. Wu, K. Sun, S. Liu, et al., "Atomically Dispersed Ni–Ru–P Interface Sites for High-Efficiency pH-Universal Electrocatalysis of Hydrogen Evolution," *Nano Energy* 80 (2021): 105467, https://doi.org/10.1016/j.nanoen.2020.105467.

61. F. Qian, L. Peng, D. Cao, et al., "Asymmetric Active Sites Originate From High-Entropy Metal Selenides by Joule Heating to Boost Electrocatalytic Water Oxidation," *Joule* 8 (2024): 2342–2356, https://doi.org/10.1016/j.joule.2024.06.004.

62. Y. Yang, K. Zhang, H. Lin, et al., "MoS_2–Ni_3S_2 Heteronanorods as Efficient and Stable Bifunctional Electrocatalysts for Overall Water Splitting," *ACS Catalysis* 7 (2017): 2357–2366, https://doi.org/10.1021/acscatal.6b03192.

63. S. Ni, H. Qu, Z. Xu, et al., "Interfacial Engineering of the $NiSe_2/FeSe_2$ p-p Heterojunction for Promoting Oxygen Evolution Reaction and Electrocatalytic Urea Oxidation," *Applied Catalysis B: Environmental* 299 (2021): 120638, https://doi.org/10.1016/j.apcatb.2021.120638.

64. A. Govind Rajan, J. M. P. Martirez, and E. A. Carter, "Facet-Independent Oxygen Evolution Activity of Pure β-NiOOH: Different Chemistries Leading to Similar Overpotentials," *Journal of the American Chemical Society* 142 (2020): 3600–3612, https://doi.org/10.1021/jacs.9b13708.

65. H.-J. Liu, S. Zhang, Y.-M. Chai, and B. Dong, "Ligand Modulation of Active Sites to Promote Cobalt-Doped 1T-MoS_2 Electrocatalytic Hydrogen Evolution in Alkaline Media," *Angewandte Chemie International Edition* 62 (2023): 202313845, https://doi.org/10.1002/anie.202313845.

66. W. Rong, Y. Chen, R. Dang, et al., "Amorphous High-Entropy IrRuCrFeCoNiO_x as Efficient Water Splitting Oxygen Evolution Reaction Electrocatalysts," *Journal of Alloys and Compounds* 971 (2024): 172786, https://doi.org/10.1016/j.jallcom.2023.172786.

67. Y. Li, L. Yang, X. Hao, et al., "Origin of Enhanced Oxygen Evolution in Restructured Metal–Organic Frameworks for Anion Exchange Membrane Water Electrolysis," *Angewandte Chemie International Edition* 64 (2025): 202413916, https://doi.org/10.1002/anie.202413916.

68. H.-J. Niu, N. Ran, W. Zhou, et al., "Synergistic Atomic Environment Optimization of Nickel–Iron Dual Sites by Co Doping and Cr Vacancy for Electrocatalytic Oxygen Evolution," *Journal of the American Chemical Society* 147 (2025): 2607–2615, https://doi.org/10.1021/jacs.4c14675.

69. H. Lei, L. Ma, Q. Wan, et al., "Promoting Surface Reconstruction of NiFe Layered Double Hydroxide for Enhanced Oxygen Evolution," *Advanced Energy Materials* 12 (2022): 2202522, https://doi.org/10.1002/aenm.202202522.

70. S. Tian, Z. Li, H. Wang, X. Du, G. Liu, and J. Li, "Phosphorus Solvation Induced Deep Reconstruction of Phosphorus-Doped Nickel-Iron Oxyhydroxides towards Efficient Oxygen Evolution Reaction," *Chemical Engineering Journal* 504 (2025): 158701, https://doi.org/10.1016/j.cej.2024.158701.

Supporting Information

Additional supporting information can be found online in the Supporting Information section.

Supporting File: adma72791-sup-0001-SuppMat.pdf.

15214095, 2026, 20, Downloaded from https://advanced.onlinelibrary.wiley.com/doi/10.1002/adma.72791 by Yonghai Cao - South China University Of Technology , Wiley Online Library on [17/11/2026]. See the Terms and Conditions (https://onlinelibrary.wiley.com/terms-and-conditions) on Wiley Online Library for rules of use; OA articles are governed by the applicable Creative Commons License